Negative magnetoresistance and spin filtering of spin-coupled di-iron-oxo clusters

Rui-Ning Wang,[1] Jorge H. Rodriguez,[2] and Wu-Ming Liu[1]

[1]*Beijing National Laboratory for Condensed Matter Physics, Institute of Physics, Chinese Academy of Sciences, Beijing 100190, China*

[2]*Department of Physics, Purdue University, West Lafayette, Indiana 47907-2036, USA*

(Received 19 June 2013; revised manuscript received 29 May 2014; published 12 June 2014)

Spin-dependent transport has been computationally studied for an open-shell singlet di-iron-oxo cluster. Currents and magnetoresistances have been investigated as a function of spin state within the nonequilibrium Green's function approach. The applied bias can be used to tune the sign of the observed magnetoresistance. A colossal magnetoresistance has been determined for hydrogen anchoring. Applied biases lower than 0.3 V, in conjunction with sulfur anchoring, induce a negative magnetoresistance due to lowering of the anchor-scatterer tunneling barrier. The di-iron-oxo cluster displays nearly perfect spin filtering for parallel alignment of the iron magnetic moments due to the energetic proximity, relative to the Fermi level, of its highest occupied molecular orbitals.

DOI: 10.1103/PhysRevB.89.235414 PACS number(s): 73.23.−b, 75.47.Gk, 85.65.+h, 85.75.−d

I. INTRODUCTION

Miniaturization of electronic devices can be aided by innovations within two disciplines, namely, spintronics [1–3] and molecular electronics [4–6]. Initially, these two disciplines did not overlap significantly [7–9]. However, more recently, a link has been established between spintronics and molecular electronics as interest has grown in the use of magnetically ordered molecular clusters for electronic transport [10–15]. For example, ferrimagnetic nanosized Fe- or Mn-based single-molecule magnets (SMMs) [16–18], which have polymetallic cores surrounded by organic ligands, have ground states with large spin and can potentially serve as magnetically functional units or logic devices [19–21]. Experimentally, spin-polarized transport of SMMs was observed with scanning tunneling microscopy and mechanically controllable break junctions [22–25], although some results remain to be theoretically clarified [26–28]. Herein, we perform computational work to study spin-polarized transport through a different and unexplored class of clusters, namely, di-iron-containing *open-shell singlets*.

In contrast to the widely studied SMMs [29–31], electronic transport by a different class of metal clusters has not been studied. Namely, spin-polarized oxygen-bridged (μO) bimetallic clusters [Fig. 1(a)] whose $S = 0$ ground state arises from antiparallel ordering of their two metal-centered magnetic moments. These systems are open-shell singlets since their ground-state multiplicity is $M = 2S + 1 = 1$ but their ground-state spin density, $\rho^S(\vec{r}) = \rho^{\uparrow}(\vec{r}) - \rho^{\downarrow}(\vec{r})$, is finite and of opposite polarity in the proximity of each of their metal centers [32], as shown in Fig. 1(d). Contrary to SMMs and certain high-spin metal complexes [33], the spin-polarized clusters studied here do not have an intrinsic magnetic anisotropy barrier due to their overall $S = 0$ ground state. Hence, we study the representative open-shell singlet shown in Fig. 1(a), herein referred to as $Fe_A{}^{3+}$-(μO)-$Fe_B{}^{3+}$, or a *di-iron-oxo* cluster [32,34], whose iron ions have a *nominal* $Fe_i{}^{3+}$ oxidation state, $S_i = 5/2$ spin ($i = A, B$), and antiparallel (AP) magnetic moments leading to a net $S = S_A - S_B = 0$ ground state. Computed iron moments are less than their *nominal* $5\mu_B$ value (Tables I and II) due to electron delocalization, resulting in small pockets of spin density on μO and their other neighboring atoms [Figs. 1(d) and 1(e)]. The μO ligand mediates superexchange interactions [32] which couple the iron atoms antiferromagnetically and provide a main conductivity channel. Thus, each iron ion is a spin center indirectly interacting with the other via their common μO ligand. The lowest and highest eigenstates of the corresponding Heisenberg Hamiltonian ($\mathcal{H}_{\mathcal{HB}} = J\vec{S}_A \cdot \vec{S}_B$) are shown in Fig. 1(b), where $J \approx +242$ cm^{-1} has been determined from magnetic susceptibility [35].

In this work, we study spin-polarized transport properties of the antiparallel magnetic-moment state as the cluster is connected to gold electrodes via hydrogen atoms [36,37]. The parallel moment (P) state is 15 J higher in energy, with a net spin $S = 5$. Thus, it was also of interest to study the differences in conductance for the low- and high-spin states. Importantly, there is no crossover [38,39] between antiparallel (low-spin) and parallel (high-spin) magnetic-moment states in the bias range (see the Supplemental Material [40]). For comparison, the cluster was also connected to gold electrodes via thiol groups, which are commonly used to build strong chemical links [41,42]. Our calculations show that parallel magnetic configurations exhibit the spin-valve effect [43,44] for both types of anchors. Finally, a negative magnetoresistance has been determined below a bias of 0.3 V [45–47] which originates in a reduced tunneling barrier.

The remainder of the paper is organized as follows. Section II describes some computational and numerical details. The main results and discussion are given in Sec. III, which includes descriptions of computed magnetic moments, colossal and negative magnetoresistances, and spin-valve effects. Finally, Sec. IV provides a brief conclusion.

II. COMPUTATIONAL METHODS

A junction was constructed where the central scatterer, $Fe_A{}^{3+}$-(μO)-$Fe_B{}^{3+}$, was modeled in both (AP and P) magnetic configurations [Fig. 1(c)]. The di-iron-oxo cluster was placed between two atomic-scale gold leads of finite cross section along the (100) direction. Terminal atoms were symmetrically anchored at the hollow site of the surface of two leads. In the initial step, the system was partially optimized via

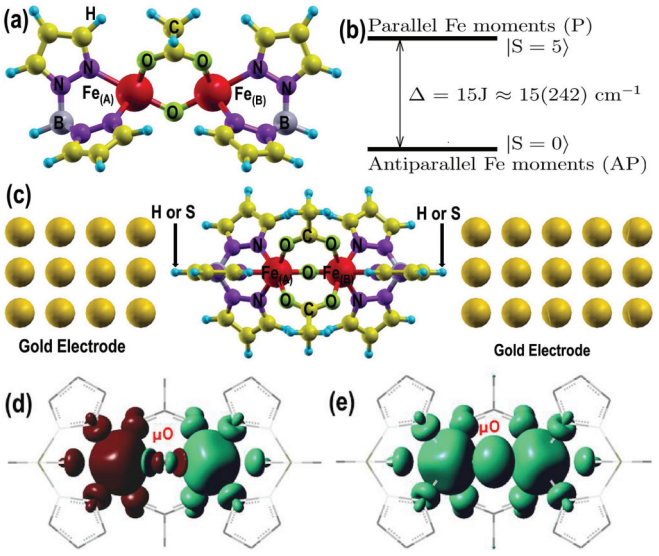

FIG. 1. (Color online) (a) Side view of $Fe_A{}^{3+}$-μO(μ-O_2CCH_3)$_2$-$Fe_B{}^{3+}$(HBpz$_3$)$_2$ cluster. (b) Highest, $|S = S_A + S_B = 5\rangle$, and lowest, $|S = S_A - S_B = 0\rangle$, eigenstates of the Heisenberg Hamiltonian. (c) Top view of cluster in contact with gold electrodes. Atom colors are iron, red; oxygen, green; nitrogen, purple; boron, gray; carbon, yellow; hydrogen, blue. (d) and (e) are computed spin densities $\rho^S(\vec{r})$ of antiparallel (AP) and parallel (P) spin states, respectively.

spin-polarized density functional theory [48] by keeping the gold electrodes frozen. Only minor differences in the cluster's geometric structure were found upon optimization with hydrogen and sulfur anchoring. A double-zeta plus polarization basis and the generalized gradient approximation parameterized by Perdew, Burke, and Ernzerhof [49] were used. Geometrical convergence was achieved when the forces were less than 0.03 eV/Å. Norm-conserving pseudopotentials [50] were constructed and used with scalar relativistic terms and core corrections following Troullier and Martins [51]. In the second stage, electronic transport was calculated with SMEAGOL [52], which combines density functional theory with the nonequilibrium Green's function formalism (see Supplemental Material) [53–56].

III. RESULTS AND DISCUSSION

A. Magnetic moments of isolated and interacting clusters

As previously mentioned, $Fe_A{}^{3+}$-(μO)-$Fe_B{}^{3+}$ is an open-shell singlet with overall ground-state spin $S = 0$. Its spin density $\rho^s(\vec{r})$ is finite and of opposite polarity in the proximity of each of its two iron centers. Each of the two iron ions has a nominal $Fe_i{}^{3+}$ oxidation state and nominal $S_i = 5/2$ spin ($i = A, B$) corresponding to magnetic moments of $5\mu_B$. However, spin density functional theory (SDFT) calculations capture valence electron delocalization effects, for example, towards the bridging oxygen atom (O3). As a result, the computed moments for each iron ion acquire values below their nominal value, whereas the moments of some adjacent atoms, such as O3 (Fig. 2) in the P configuration, become non-negligible and finite. The magnetic moments of selected atoms, computed within the Mulliken framework, are shown in

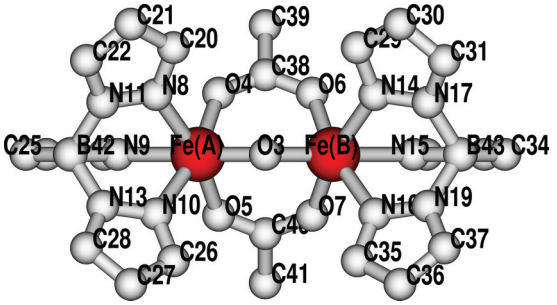

FIG. 2. (Color online) Geometric structure and atomic labels of the di-iron-oxo cluster. Gold and hydrogen atoms not shown. The central (bridging) oxygen atom is interchangeably labeled μO and O3 in this work.

Tables I and II as a function of applied bias. As shown in the tables, regardless of applied bias, the sum of the atomic moments associated with the iron atoms and those atoms (five in each case) chemically bound to them (partial total) approach the nominal values of 0 and 10, corresponding to antiparallel (AP) and parallel (P) configurations, respectively. The remaining minimal contributions (not shown) are localized on the other atomic centers of the cluster. Importantly, for both hydrogen and sulfur anchoring, the sum of moments for all gold atoms in left and right electrodes is essentially zero.

Mainly due to $Fe_{A,B} \leftrightarrow$ O3 valence electron delocalization, the iron magnetic moments are greater than $4\mu_B$ but lower than their nominal value of $5\mu_B$. However, atoms chemically bound to the iron atoms (O4-O7, N8-N10, N14-N16) concomitantly carry small moments ($\approx$0.03–0.85μ_B) whose magnitudes are slightly dependent on the cluster's magnetic configuration (AP or P), atomic chemical environment, and applied voltage. The case of the bridging O3 is particularly interesting since $Fe_{A,B} \leftrightarrow$ O3 delocalization in the AP and P configurations has opposite effects on its net magnetic moment. In the AP configuration the nominal C_2v symmetry of the di-iron-oxo cluster ensures equal degrees of electron delocalization associated with $Fe_A \leftrightarrow$ O3 and $Fe_B \leftrightarrow$ O3 but opposite spin polarity. As a result, for the AP state the computed moments of O3 are nearly zero. By contrast, in the P configuration, the delocalized electron densities corresponding to $Fe_A \leftrightarrow$ O3 and $Fe_B \leftrightarrow$ O3 are of the same spin polarity, and their combined contributions lead to an O3 moment of $\approx 0.6\mu_B$.

The magnitude of the moments remained nearly the same with increasing bias except in the 0.8–1.0 V bias range, where some decrease in magnitude is seen (Fig. 3). This effect is particularly true for the P states. The iron moments corresponding to P states were slightly larger than those of AP states. The magnetic moments of each metal in the di-iron cluster with H anchoring were slightly greater than those corresponding to S anchoring. This behavior is consistent with stronger cluster-electrode electronic coupling for S anchoring, which favors greater electron delocalization between the electrodes and the cluster.

B. Colossal and negative magnetoresistances

Spin-polarized currents were self-consistently calculated within the nonequilibrium Green's function approach with the

TABLE I. Selected atomic magnetic moments for antiparallel (AP) and parallel (P) spin configurations as a function of applied bias for H anchoring (units of μ_B).

	0.0 V		0.2 V		0.4 V		0.6 V		0.8 V		1.0 V	
Atom	AP	P	AP	P	AP	P	AP	P	AP	P	AP	P
O3 (μO)[a]	+0.003	+0.653	−0.001	+0.648	−0.005	+0.637	−0.009	+0.624	−0.013	+0.609	−0.018	+0.58
Fe1	+4.145	+4.269	+4.146	+4.269	+4.148	+4.264	+4.148	+4.257	+4.149	+4.248	+4.151	+4.217
O4	+0.050	+0.083	+0.049	+0.084	+0.049	+0.083	+0.048	+0.083	+0.049	+0.082	+0.048	+0.080
O5	+0.049	+0.083	+0.049	+0.082	+0.048	+0.083	+0.048	+0.083	+0.048	+0.082	+0.048	+0.079
N8	+0.032	+0.038	+0.032	+0.038	+0.033	+0.039	+0.033	+0.039	+0.034	+0.039	+0.034	+0.037
N9	+0.050	+0.055	+0.051	+0.055	+0.051	+0.055	+0.051	+0.056	+0.051	+0.056	+0.051	+0.055
N10	+0.050	+0.055	+0.050	+0.055	+0.051	+0.055	+0.051	+0.055	+0.051	+0.056	+0.051	+0.054
Fe2	−4.147	+4.271	−4.145	+4.265	−4.144	+4.257	−4.141	+4.250	−4.139	+4.242	−4.136	+4.218
O6	−0.051	+0.082	−0.052	+0.083	−0.052	+0.083	−0.051	+0.082	−0.052	+0.082	−0.052	+0.081
O7	−0.051	+0.082	−0.051	+0.082	−0.052	+0.082	−0.051	+0.082	−0.051	+0.082	−0.052	+0.080
N14	−0.049	+0.053	−0.049	+0.053	−0.048	+0.053	−0.048	+0.052	−0.048	+0.051	−0.047	+0.050
N15	−0.048	+0.052	−0.048	+0.052	−0.047	+0.052	−0.047	+0.052	−0.047	+0.051	−0.047	+0.050
N16	−0.031	+0.036	−0.031	+0.035	−0.030	+0.035	−0.029	+0.034	−0.028	+0.034	−0.028	+0.032
Partial total[b]	−0.045	+9.812	+0.000	+9.801	+0.002	+9.778	+0.003	+9.749	+0.004	+9.714	+0.003	+9.613
All Au (LE)[c]	−0.005	−0.012	−0.007	−0.055	−0.000	−0.015	−0.003	−0.011	−0.001	−0.012	−0.001	−0.016
All Au (RE)[d]	+0.000	−0.011	+0.001	−0.011	+0.001	−0.010	+0.001	−0.012	+0.005	−0.010	+0.001	−0.008

[a]The central (bridging) oxygen atom is referred to as both μO and O3 in this work.
[b]Sum of moments of the (13) atoms shown above. Does not include all atoms in the di-iron cluster.
[c]Sum of moments of all gold atoms in the left electrode (LE).
[d]Sum of moments of all gold atoms in the right electrode (RE).

voltage-dependent Landauer-Büttike formula,

$$I_\sigma = \frac{e}{h}\int_{\mu_L}^{\mu_R} T_\sigma(E,V)[f_L(E-\mu_L) - f_R(E-\mu_R)]dE,$$

where $\sigma = \uparrow$ or $\downarrow$, $f_{L,R}(E) = 1/(1+e^{\frac{E-\mu_{L,R}}{k_BT}})$ are the Fermi-Dirac distributions, and $\mu_{L,R}$ are the chemical potentials for the left and right electrodes, respectively. $T_\sigma(E,V) = \mathrm{Tr}[\mathrm{Im}(\Sigma_L^r)G^r Im(\Sigma_R^r)G^a]$ are the spin-dependent transmission coefficients. Self-consistent currents for the AP and P configurations of $Fe_A{}^{3+}$-(μO)-$Fe_B{}^{3+}$ in contact with gold electrodes with hydrogen and sulfur anchoring are shown in Figs. 4(a) and 4(b), respectively. The currents of the higher-energy P states were about two (hydrogen anchoring)

TABLE II. Selected atomic magnetic moments for antiparallel (AP) and parallel (P) spin configurations as a function of applied bias for S anchoring (units of μ_B).

	0.0 V		0.2 V		0.4 V		0.6 V		0.8 V		1.0 V	
Atom	AP	P	AP	P	AP	P	AP	P	AP	P	AP	P
O3 (μO)[a]	+0.007	+0.654	+0.003	+0.654	−0.001	+0.651	−0.006	+0.643	−0.011	+0.627	−0.015	+0.616
Fe1	+4.090	+4.247	+4.091	+4.249	+4.091	+4.249	+4.092	+4.244	+4.092	+4.230	+4.091	+4.197
O4	+0.056	+0.085	+0.055	+0.084	+0.055	+0.085	+0.055	+0.084	+0.054	+0.083	+0.054	+0.084
O5	+0.055	+0.082	+0.054	+0.081	+0.054	+0.081	+0.054	+0.081	+0.053	+0.079	+0.053	+0.080
N8	+0.035	+0.045	+0.036	+0.046	+0.036	+0.046	+0.037	+0.047	+0.037	+0.047	+0.037	+0.048
N9	+0.054	+0.062	+0.054	+0.062	+0.055	+0.062	+0.055	+0.063	+0.055	+0.063	+0.056	+0.063
N10	+0.053	+0.060	+0.053	+0.061	+0.053	+0.060	+0.054	+0.061	+0.054	+0.060	+0.054	+0.062
Fe2	−4.092	+4.251	−4.092	+4.248	−4.091	+4.244	−4.089	+4.238	−4.087	+4.225	−4.085	+4.193
O6	−0.057	+0.080	−0.056	+0.081	−0.057	+0.080	−0.057	+0.080	−0.057	+0.080	−0.057	+0.081
O7	−0.058	+0.084	−0.057	+0.084	−0.058	+0.084	−0.059	+0.084	−0.058	+0.084	−0.059	+0.083
N14	−0.051	+0.058	−0.051	+0.057	−0.050	+0.057	−0.050	+0.057	−0.050	+0.056	−0.050	+0.056
N15	−0.054	+0.061	−0.054	+0.061	−0.053	+0.061	−0.053	+0.060	−0.053	+0.060	−0.053	+0.060
N16	−0.036	+0.045	−0.035	+0.044	−0.034	+0.043	−0.034	+0.042	−0.034	+0.041	−0.033	+0.041
Partial total[b]	+0.002	+9.814	+0.001	+9.812	+0.000	+9.803	−0.001	+9.784	−0.005	+9.735	−0.007	+9.664
All Au(LE)[c]	+0.002	+0.002	+0.001	−0.001	+0.001	+0.001	−0.001	−0.002	+0.000	−0.009	+0.000	−0.005
All Au(RE)[d]	+0.002	+0.003	+0.003	+0.002	+0.002	+0.003	−0.001	+0.008	+0.002	+0.007	+0.001	+0.007

[a]The central (bridging) oxygen atom is referred to as both μO and O3 in this work.
[b]Sum of moments of the (13) atoms shown above. Does not include all atoms in the di-iron cluster.
[c]Sum of moments of all gold atoms in the left electrode (LE).
[d]Sum of moments of all gold atoms in the right electrode (RE).

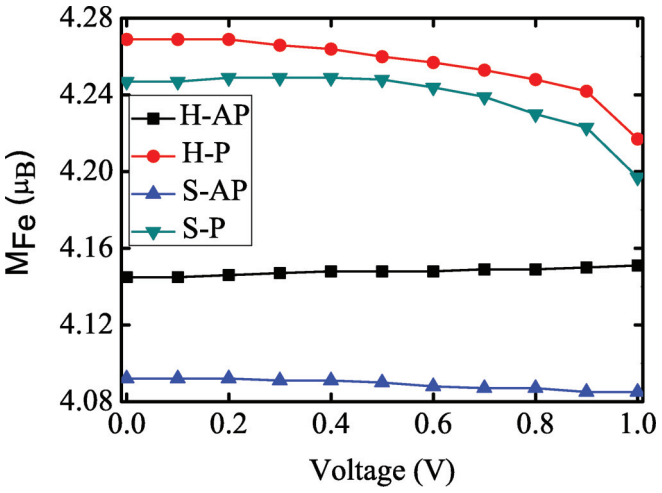

FIG. 3. (Color online) Magnetic moments of iron atoms in P and AP magnetic-moment states with hydrogen and sulfur anchoring in the bias range of [0, 1] V. The red line with solid dots (H-P) corresponds to moments of each iron atom in the parallel states with hydrogen anchoring. The black line with solid squares (H-AP) represents the moments of each iron atom in the antiparallel state with hydrogen anchoring. The green line with inverted triangles (S-P) represents the moments in parallel states with sulfur anchoring. The blue line with triangles (S-AP) represents the moments in antiparallel states with sulfur anchoring.

or one (sulfur anchoring) orders of magnitude larger than those of their corresponding AP states for a 1.0 V bias. Thus, overall, the parallel moment states displayed much better conductivity. This is consistent with the high degree of $Fe_A \leftrightarrow (\mu O) \leftrightarrow Fe_B$ delocalization of the di-iron-oxo cluster's highest occupied molecular orbitals (HOMOs) in its parallel configuration [32]. The development of spintronic devices based on giant magnetoresistances (MR) [57–59]

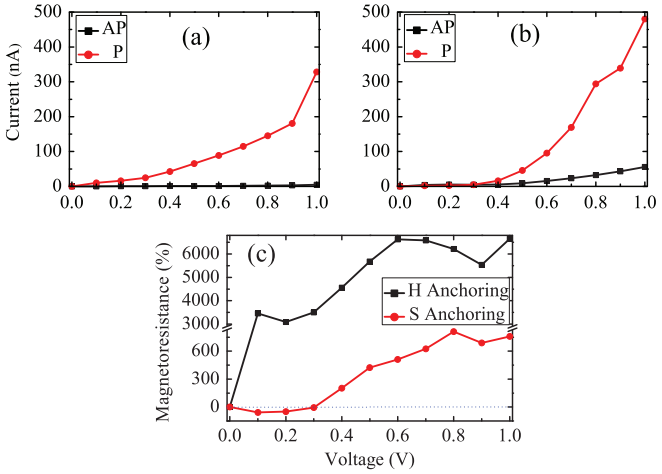

FIG. 4. (Color online) Transport properties of Fe^{3+}-(μO)-$Fe^{3+}(HBpz_3)_2$ in contact with electrodes. Current-voltage profiles for AP (black line with solid squares) and P (red line with solid dots) alignments with (a) hydrogen or (b) sulfur atoms as the anchoring groups. (c) Magnetoresistance for sulfur (red line with solid dots) and hydrogen (black line with solid squares) anchoring.

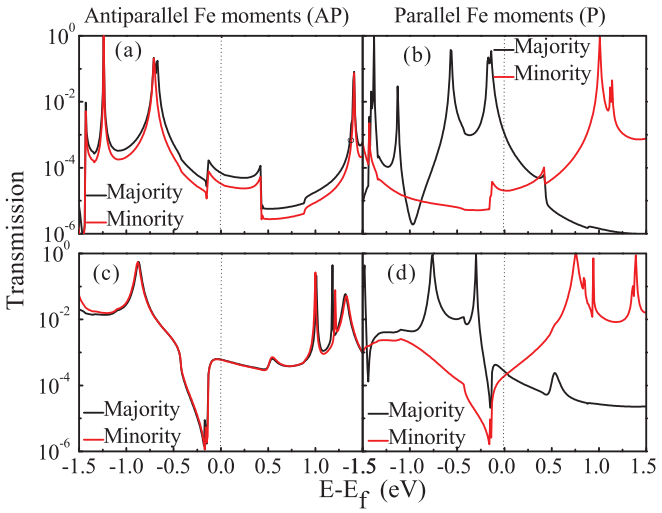

FIG. 5. (Color online) Logarithm of the spin-resolved (black line, majority spin; red line, minority spin) transmission spectra for (left) antiparallel and (right) parallel alignments of magnetization with (a) and (b) hydrogen anchoring and (c) and (d) sulfur anchoring under the zero bias.

has revolutionized the magnetic memory industry. From the predicted current-voltage profiles we can infer a MR ratio defined in terms of the currents associated with AP and P states, $MR = (I_P - I_{AP})/I_{AP}$, which imposes no upper bound and is shown in Fig. 4(c). For hydrogen anchoring, the MR ratio increased from 0.2 to 0.6 V and reached a maximum (~6000%) at 0.6 V. Thus, the di-iron-oxo cluster displayed a colossal MR effect. For sulfur anchoring, the MR ratio was less than zero in the low-bias zone (0–0.3 V), and the di-iron-oxo junction showed a negative MR effect, indicating that the current associated with the AP state is greater than that of the P state. Above a 0.3 V bias, the MR ratio tended to increase with increasing bias for sulfur anchoring. However, the MR ratio for sulfur anchoring was somewhat lower than that of hydrogen anchoring, which quickly increased to a saturation value. The colossal MR effect associated with hydrogen anchoring can be explained in terms of the transmission spectra, as shown in Figs. 5(a) and 5(b), and the cluster's density of states (see Supplemental Material).

The significant difference between the transport properties of AP and P states may be rationalized in terms of their transmission spectra. Figure 5 exhibits features which strongly depend on the relative orientation (AP or P) of the magnetic moments of the irons. For both magnetic configurations the transmission probabilities decay rapidly when the energy falls below that of the lowest unoccupied molecular orbital (LUMO) or rises above that of the HOMOs. The molecular orbitals are fairly localized within the di-iron-oxo cluster because it is weakly coupled to the gold electrodes [60]. In the weak-coupling limit, transport occurs when one molecular orbital is shifted to the Fermi level E_f of the leads. Experimentally, the molecular orbital energies can be tuned by the gate voltage [61]. In the present system, such effect is obtained by changing the relative orientation of the magnetic moments of the iron ions. Parallel alignment, in conjunction with hydrogen anchoring, decreases the HOMO-LUMO gap

TABLE III. Energies of HOMO and LUMO for AP and P alignments for hydrogen and sulfur anchoring and the ratio of majority-spin to minority-spin transmission, $(T_{\text{majority}} - T_{\text{minority}})/T_{\text{minority}}$, computed at the HOMO energy.

	H anchoring		S anchoring	
	AP	P	AP	P
HOMO (eV)	−0.71	−0.14	−0.87	−0.30
LUMO (eV)	+1.41	+1.01	+1.01	+0.76
$\frac{T_{\text{majority}}-T_{\text{minority}}}{T_{\text{minority}}}$	4.29×10^{-2}	2.35×10^{4}	1.65×10^{-1}	5.50×10^{4}

from 2.12 eV (for AP) to 1.15 eV. Reminiscent of scanning tunneling spectroscopy observations for Mn_{12} single-molecule magnets [29], the electronic transport through the di-iron-oxo cluster mainly occurs via the (P) HOMO, which is in energetic proximity (−0.14 eV) to E_f (Table III). Accordingly, the P configuration has much better conductivity properties than the AP configuration, whose HOMO is at −0.71 eV. Therefore, $Fe_A{}^{3+}$-(μO)-$Fe_B{}^{3+}$ shows an essentially perfect colossal MR with potential use as a magnetic memory unit.

For sulfur anchoring, the P configuration leads to features similar to those of hydrogen anchoring. Namely, the HOMO-LUMO gap decreases from 1.88 eV in the AP arrangement to 1.06 eV, and the HOMO level is shifted, relative to E_f, from −0.87 to −0.30 eV [Figs. 5(c) and 5(d) and Table III]. However, for sulfur anchoring, a negative MR effect is observed which is not directly understood from the transmission spectra alone. For density functional calculations, the self-consistently calculated properties are dependent on the exchange-correlation (xc) and other potentials. Therefore, to rationalize the negative MR, one can consider the xc potentials associated with majority-spin ($V_{\text{xc}}^{\text{majority}}$) and minority-spin ($V_{\text{xc}}^{\text{minority}}$) electrons. The planar average potentials along the transport direction are shown in Fig. 6. Compared to AP alignments, the P configurations result in similar changes of xc potentials when the di-iron-oxo cluster is anchored through hydrogen or sulfur anchoring, as shown in Figs. 6(a) and 6(b). For the AP alignment, along the transport direction, the difference xc potential ($V_{\text{xc}}^{\text{majority}} - V_{\text{xc}}^{\text{minority}}$) first meets a shallow potential well and then a high potential barrier. By contrast, for the P alignment, the difference xc potential first meets a low potential barrier and then a deep potential well. Therefore, for the P alignment, the majority carriers will scatter on two potential wells around the iron ions during conduction. In contrast, the minority carriers traverse through two potential barriers. The absolute magnitudes of the main potential wells and barriers are nearly the same for the AP and P configurations due to the nominal C_{2v} molecular symmetry.

The total potential includes, in addition to the Hartree (h) and xc components, the pseudopotential (pseudo) representing core electrons ($V_T = V_h + V_{\text{xc}} + V_{\text{pesudo}}$). The negative MR effect observed for sulfur anchoring may be attributed to the corresponding total potential becoming more negative (within the junction region) relative to hydrogen anchoring, as shown in Fig. 6(c). The current through the molecular junction not only depends on the intrinsic electronic structure of the di-iron-oxo cluster but also on its anchor-dependent, interfacial barrier. When hydrogen anchoring is replaced by

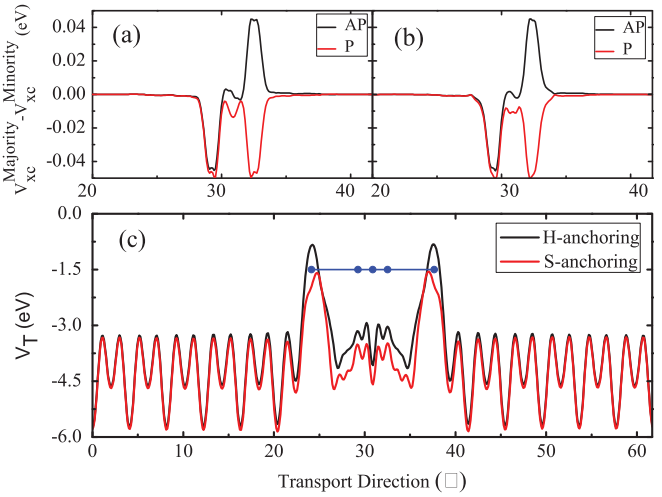

FIG. 6. (Color online) Planar average potentials in AP (black line) and P (red line) states along the transport direction of the di-iron-oxo molecular junction. (a) and (b) Difference in xc potentials associated with majority- and minority-spin electrons, $V_{\text{xc}}^{\text{majority}} - V_{\text{xc}}^{\text{minority}}$, for hydrogen and sulfur anchoring, respectively. (c) Total potentials V_T of the cluster in contact with the electrodes for hydrogen and sulfur anchoring. Blue dots are at the locations of the left anchoring atom, left iron, linking oxygen, right iron, and right anchoring atom.

sulfur anchoring, the current increases (Fig. 4) due to the lower total interfacial potential [62,63]. However, for AP alignment, such an anchor-dependent potential decrease makes the current increase by about one order of magnitude in the higher-bias region ($\leqslant$1.0 V), up to $\approx$50 nA. For P alignment, in the higher-bias region ($\leqslant$1.0 V), the same anchoring substitution gives rise to a lesser relative increment in the current (about a factor of 2) but to a much greater absolute increment, roughly from 300 to 500 nA (Fig. 4). Relative to the low-bias region ($\geqslant$0.0 V), the net increment in the current as a function of bias is much more pronounced for AP $\rightarrow$ P realignment than for H $\rightarrow$ S substitution. An AP $\rightarrow$ P reorientation of the iron magnetic moments is concomitant with substantial changes in the cluster's electronic structure [32]. Therefore, the current is dominated by the anchor-dependent tunneling barrier at lower voltages and by the magnetic alignment (AP or P) at higher voltages.

C. Spin-valve effect

Figures 5(a) and 5(c) show that near E_f the transmissions for majority and minority spins are essentially equal for AP configurations. This is true for either type of anchoring. For parallel magnetic-moment states [Figs. 5(b) and 5(d)], however, the transmissions near E_f for majority spin dominate. This effect is further illustrated by the ratios of majority-spin to minority-spin transmission coefficients, $(T_{\text{majority}} - T_{\text{minority}})/T_{\text{minority}}$, computed at the energy of the HOMO level. Table III shows that these ratios for P configurations are orders of magnitude larger than those of their AP counterparts. This is consistent with plots of the partial density of states displaying intensities closer to E_f for P states compared to AP states (see the Supplemental Material). The previous features of

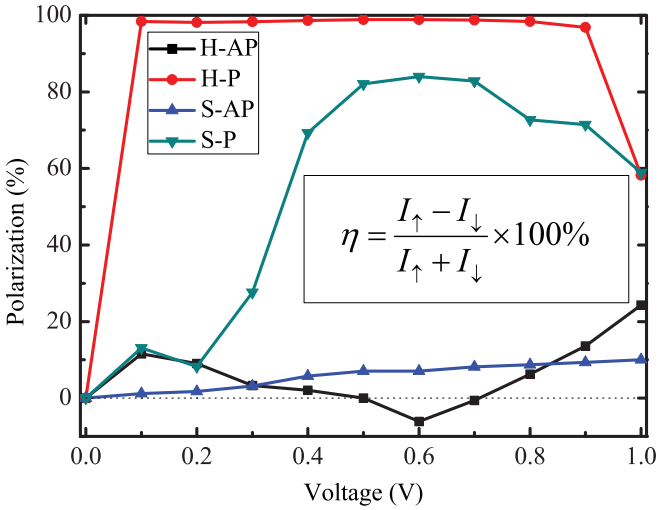

FIG. 7. (Color online) Polarization of the current through Fe^{3+}-(μO)-$Fe^{3+}(HBpz_3)_2$ as a function of bias for the AP or P alignment for hydrogen and sulfur anchoring.

the transmission spectra point to preferential transmission of majority-spin electrons and thus to effective spin filtering. The polarization of the current can also be analyzed in terms of the spin-injection factor $\eta = (I_\uparrow - I_\downarrow)/(I_\uparrow + I_\downarrow) \times 100\%$. The polarization of the current as a function of the bias and anchor is shown in Fig. 7. For AP states the currents are not strongly spin polarized. However, η significantly increases for P states, particularly for hydrogen anchoring, where η is on the order of ~95% in the bias range 0.1–0.9 V. This indicates that $Fe_A{}^{3+}$-(μO)-$Fe_B{}^{3+}$ in its P configuration may be used in the context of molecular spintronics to achieve an excellent spin-filtering effect. This is particularly true at higher temperatures, for which the P configuration is significantly populated.

IV. CONCLUSION

Either colossal or negative magnetoresistances have been computed for the sulfur-anchored di-iron-oxo cluster depending on the applied bias. A spin-valve effect has been predicted for the parallel moment states, in particular for hydrogen anchoring, for which the polarization of the current is on the order of 95% over a range of applied bias. This suggests achieving control of different transport properties of the same molecular cluster by tuning the applied bias in the context of molecular spintronic devices.

ACKNOWLEDGMENTS

Grants partially supporting this work are as follows: China Postdoctoral Science Foundation Grant No. 2013M530756 (R.-N.W.), NKBRSFC (W.-M.L.) Grants No. 2011CB921502 and No. 2012CB821305, NSFC (W.-M.L.) Grants No. 61227902 and No. 61378017, and NSF Grant No. CHE-0349189 (J.H.R.).

[1] S. A. Wolf, D. D. Awschalom, R. A. Buhrman, J. M. Daughton, S. von Molnár, M. L. Roukes, A. Y. Chtchelkanova, and D. M. Treger, Science **294**, 1488 (2001).
[2] A. Fert, Rev. Mod. Phys. **80**, 1517 (2008).
[3] P.-B. He, X. C. Xie, and W. M. Liu, Phys. Rev. B **72**, 172411 (2005).
[4] W. Wang, T. Lee, and M. A. Reed, Phys. Rev. B **68**, 035416 (2003).
[5] A. Aviram and M. A. Ratner, Chem. Phys. Lett. **29**, 277 (1974).
[6] C. Joachim, J. K. Gimzewski, and A. Aviram, Nature (London) **408**, 541 (2000).
[7] H. Song, M. A. Reed, and T. Lee, Adv. Mater. **23**, 1583 (2011).
[8] J. Shi, P. Zhang, D. Xiao, and Q. Niu, Phys. Rev. Lett. **96**, 076604 (2006).
[9] J. H. Rodriguez, J. Chem. Phys. **123**, 094709 (2005).
[10] A. R. Rocha, V. M. García-suárez, S. W. Bailey, C. J. Lambert, J. Ferrer, and S. Sanvito, Nat. Mater. **4**, 335 (2005).
[11] M. Urdampilleta, S. Klyatskaya, J.-P. Cleuziou, M. Ruben, and W. Wernsdorfer, Nat. Mater. **10**, 502 (2011).
[12] T. Miyamachi, M. Gruber, V. Davesne, M. Bowen, S. Boukari, L. Joly, F. Scheurer, G. Rogez, T. K. Yamada, P. Ohresser *et al.*, Nat. Commun. **3**, 938 (2012).
[13] D. Aravena and E. Ruiz, J. Am. Chem. Soc. **134**, 777 (2012).
[14] J. Ferrer and V. M. García-Suárez, J. Mater. Chem. **19**, 1696 (2009).
[15] C. Ni, S. Shah, D. Hendrickson, and P. R. Bandaru, Appl. Phys. Lett. **89**, 212104 (2006).
[16] A. Caneschi, D. Gatteschi, R. Sessoli, A. L. Barra, L. C. Brunel, and M. Guillot, J. Am. Chem. Soc. **113**, 5873 (1991).
[17] H. J. Eppley, H.-L. Tsai, N. de Vries, K. Folting, G. Christou, and D. N. Hendrickson, J. Am. Chem. Soc. **117**, 301 (1995).
[18] T. Lis, Acta Crystallogr., Sect. B **36**, 2042 (1980).
[19] L. Bogani and W. Wernsdorfer, Nat. Mater. **7**, 179 (2008).
[20] R. Sessoli, D. Gatteschi, A. Caneschi, and M. A. Novak, Nature (London) **365**, 141 (1993).
[21] C. D. Pemmaraju, I. Rungger, and S. Sanvito, Phys. Rev. B **80**, 104422 (2009).
[22] F. Prins, M. Monrabal-Capilla, E. A. Osorio, E. Coronado, and H. S. J. van der Zant, Adv. Mater. **23**, 1545 (2011).
[23] V. Meded, A. Bagrets, K. Fink, R. Chandrasekar, M. Ruben, F. Evers, A. Bernand-Mantel, J. S. Seldenthuis, A. Beukman, and H. S. J. van der Zant, Phys. Rev. B **83**, 245415 (2011).
[24] M. S. Alam, M. Stocher, K. Gieb, P. Müller, M. Haryono, K. Student, and A. Grohmann, Angew. Chem. Int. Ed. **49**, 1159 (2010).
[25] S. Voss, M. Fonin, U. Rüdinger, M. Burgert, and U. Groth, Appl. Phys. Lett. **90**, 133104 (2007).
[26] H. B. Heersche, Z. de Groot, J. A. Folk, H. S. J. van der Zant, C. Romeike, M. R. Wegewijs, L. Zobbi, D. Barreca, E. Tondello, and A. Cornia, Phys. Rev. Lett. **96**, 206801 (2006).
[27] S. Barraza-Lopez, K. Park, V. García-Suárez, and J. Ferrer, Phys. Rev. Lett. **102**, 246801 (2009).
[28] S. Barraza-Lopez, K. Park, V. García-Suárez, and J. Ferrer, J. Appl. Phys. **105**, 07E309 (2009).

[29] S. Voss, O. Zander, M. Fonin, U. Rüdiger, M. Burgert, and U. Groth, Phys. Rev. B **78**, 155403 (2008).
[30] K. Park, S. Barraza-Lopez, V. M. García-Suárez, and J. Ferrer, Phys. Rev. B **81**, 125447 (2010).
[31] G.-H. Kim and T.-S. Kim, Phys. Rev. Lett. **92**, 137203 (2004).
[32] J. H. Rodriguez and J. K. McCusker, J. Chem. Phys. **116**, 6253 (2002).
[33] F. Aquino and J. H. Rodriguez, J. Phys. Chem. A **113**, 9150 (2009).
[34] W. H. Armstrong and S. J. Lippard, J. Am. Chem. Soc. **105**, 4837 (1983).
[35] W. H. Armstrong, A. Spool, G. C. Papaefthymiou, R. B. Frankel, and S. J. Lippard, J. Am. Chem. Soc. **106**, 3653 (1984).
[36] D. Djukic, K. S. Thygesen, C. Untiedt, R. H. M. Smit, K. W. Jacobsen, and J. M. van Ruitenbeek, Phys. Rev. B **71**, 161402(R) (2005).
[37] M. L. Trouwborst, E. H. Huisman, S. J. van der Molen, and B. J. van Wees, Phys. Rev. B **80**, 081407(R) (2009).
[38] M. Chattopadhyaya, Md. M. Alam, S. Sen, and S. Chakrabarti, Phys. Rev. Lett. **109**, 257204 (2012).
[39] H. Hao, X. H. Zheng, L. L. Song, R. N. Wang, and Z. Zeng, Phys. Rev. Lett. **108**, 017202 (2012).
[40] See Supplemental Material at http://link.aps.org/supplemental/10.1103/PhysRevB.89.235414 for plots of density of states and summary of Green's function formalism.
[41] B. Xu and N. J. Tao, Science **301**, 1221 (2003).
[42] M. Mannini, D. Bonacchi, L. Zobbi, F. M. Piras, E. A. Speets, A. Caneschi, A. Cornia, A. Magnani, B. J. Ravoo, D. N. Reinhoudt *et al.*, Nano Lett. **5**, 1435 (2005).
[43] Z.-D. Li, Q.-Y. Li, L. Li, and W. M. Liu, Phys. Rev. E **76**, 026605 (2007).
[44] A. Aharony, Y. Tokura, G. Z. Cohen, O. Entin-Wohlman, and S. Katsumoto, Phys. Rev. B **84**, 035323 (2011).
[45] V. K. Dugaev, M. Inglot, E. Y. Sherman, J. Berakdar, and J. Barnas, Phys. Rev. Lett. **109**, 206601 (2012).
[46] K. Yoshida, L. Hamada, S. Sakata, A. Umeno, M. Tsukada, and K. Hirakawa, Nano Lett. **13**, 481 (2013).
[47] V. N. Smolyaninova, X. C. Xie, F. C. Zhang, M. Rajeswari, R. L. Greene, and S. Das Sarma, Phys. Rev. B **62**, 3010 (2000).
[48] J. M. Soler, E. Artacho, J. Gale, D. A. Garacia, J. Junquera, P. Ordejon, and D. Sanchez-Portal, J. Phys.: Condens. Matter **14**, 2745 (2002).
[49] J. P. Perdew, K. Burke, and M. Ernzerhof, Phys. Rev. Lett. **77**, 3865 (1996).
[50] D. R. Hamann, M. Schlüter, and C. Chiang, Phys. Rev. Lett. **43**, 1494 (1979).
[51] N. Troullier and J. L. Martins, Phys. Rev. B **43**, 1993 (1991).
[52] A. R. Rocha, V. M. García-Suárez, S. Bailey, C. Lambert, J. Ferrer, and S. Sanvito, Phys. Rev. B **73**, 085414 (2006).
[53] A.-P. Jauho, N. S. Wingreen, and Y. Meir, Phys. Rev. B **50**, 5528 (1994).
[54] J. Taylor, H. Guo, and J. Wang, Phys. Rev. B **63**, 245407 (2001).
[55] B. Wang, J. Wang, and H. Guo, Phys. Rev. Lett. **82**, 398 (1999).
[56] S. Datta, Superlattices Microstruct. **28**, 253 (2000).
[57] M. N. Baibich, J. M. Broto, A. Fert, F. N. V. Dau, F. Petroff, P. Eitenne, G. Creuzet, A. Friederich, and J. Chazelas, Phys. Rev. Lett. **61**, 2472 (1988).
[58] Y.-T. Zhang, H. Jiang, Q.-F. Sun, and X. C. Xie, Phys. Rev. B **81**, 165404 (2010).
[59] S. A. Yang, Q. Niu, D. A. Pesin, and A. H. MacDonald, Phys. Rev. B **82**, 184402 (2010).
[60] S. Barraza-Lopez, M. C. Avery, and K. Park, Phys. Rev. B **76**, 224413 (2007).
[61] T. M. Perrine and B. D. Dunietz, J. Am. Chem. Soc. **132**, 2914 (2010).
[62] V. M. García-Suárez, A. R. Rocha, S. W. Bailey, C. J. Lambert, S. Sanvito, and J. Ferrer, Phys. Rev. B **72**, 045437 (2005).
[63] I. S. Kristensen, M. Paulsson, K. S. Thygesen, and K. W. Jacobsen, Phys. Rev. B **79**, 235411 (2009).